ALMA MEMO 332

PHASE CORRECTION OF INTERFEROMETER DATA AT MAUNA KEA AND CHAJNANTOR

Guillermo Delgado
Onsala Space Observatory / European Southern Observatory
Casilla 19001, Santiago 19, Chile
Email: gdelgado@eso.org

Angel Otárola
European Southern Observatory
Casilla 19001, Santiago 19, Chile
Email: aotarola@eso.org

Lars-Åke Nyman
Onsala Space Observatory / European Southern Observatory
Casilla 19001, Santiago 19, Chile
Email: lnyman@eso.org

Roy Booth
Onsala Space Observatory
S-43992 Onsala, Sweden
Email: roy@oso.chalmers.se

Victor Belitsky
Onsala Space Observatory
Radio and Space Science, S-41296 Göteborg, Sweden
Email: belitsky@oso.chalmers.se

Denis Urbain
Onsala Space Observatory
Radio and Space Science, S-41296 Göteborg, Sweden
Email: denis@oso.chalmers.se

Richard Hills
Mullard Radio Astronomy Observatory
Cavendish Laboratory, Cambridge CB3 OHE, UK
Email: richard@mrao.cam.ac.uk

Yasmin Robson
Mullard Radio Astronomy Observatory
Cavendish Laboratory, Cambridge CB3 OHE, UK
Email: yr@astro.ox.ac.uk

Pierre Martin-Cocher
Mullard Radio Astronomy Observatory / ASIAA
P.O. Box 1-87, Nankang Taipei, 11 529 Taiwan
Email: pierre@asiaa.sinica.edu.tw

Abstract – We describe here a method to correct interferometer phase variations due to fluctuations in the atmospheric water vapour. The fluctuations are estimated by fitting an atmospheric water line model to antenna temperature values measured at frequencies near the water vapour line at 183 GHz. The fitting is done with the atmospheric water vapour density as a variable, iterating until agreement between observation and prediction is achieved. From the computed value of water vapour density, an integrated value for the precipitable water vapour (*PWV*) contained in the atmospheric column is derived.

The variations on the amount of *PWV* are directly related to electrical path length variations of an electromagnetic wave travelling through the atmosphere. This quantity, at millimetre and sub-millimetre frequencies, can be linearly related to a phase variation in an astronomical signal arriving to the elements of an interferometer.

This method to estimate the *PWV* has been used before to analyse the data from a 183 GHz radiometer operating at Llano de Chajnantor, the selected site for the Atacama Large Millimeter Array (ALMA), creating a time series of the *PWV* in the area. The derived values have been previously correlated with observations of atmospheric opacity at 225 GHz and radiosonde measurements, with good results [1].

Here we apply this radiometric method of phase variation estimation to two real cases. One is the data from interferometric observations at Mauna Kea between the James Clark Maxwell Telescope (JCMT) and the Caltech Submillimeter Observatory (CSO), operating at 356 GHz. The second case is at Chajnantor, where we have a 300-m baseline interferometer operating at 11.2 GHz. In both cases we compare the phase estimated by radiometry and the interferometer phase. Figures for correlation and achieved phase correction are given. Some error sources are discussed.

1 Introduction

To a first order approximation, water vapour distributes exponentially in the troposphere but, because water vapour is not well mixed, it is moved by the predominant winds in bubbles or patches, generally trapped in well-defined layers of the atmosphere. The size of these water vapour structures is such that phase changes occur, in time scales of a few seconds, when the disturbance crosses in front of the elements of an interferometer.

Phase fluctuations in millimetre and submillimetre interferometric observations produce a loss in resolution and decreases the signal strength. A proposed method to correct the phase fluctuations is to estimate the amount of *PWV* in the observed column of atmosphere, and to use this value to determine the excess path delay. Measuring the variability of the *PWV*, at each element of an interferometer, a relative phase difference can be determined, and this value can be used to remove the interferometer phase fluctuation.

Different methods are available to retrieve the precipitable water vapour content of the atmosphere from ground based observations [2]. However, not all of them are suitable for our application, which needs continuous, sensitive, and nearly real time measurements with little or no supervision and in the same direction as the incoming astronomical signal. Here we present a detailed description of a method to estimate the amount of *PWV* based on measurements of antenna temperatures at different frequencies near the 183 GHz water line with a radiometer. These values are compared with the output of an atmospheric model that predicts the 183 GHz water line intensity for different values of water vapour density. The water vapour density is iterated until agreement is achieved with the measured antenna temperatures. The best-fitting water vapour density value is integrated to obtain a value for *PWV* and, from this value, the associated electrical pathlength. Since the atmosphere is highly non-dispersive at these frequencies, the electrical pathlength variations translate directly to phase variations at any given frequency.

Here we present this type of phase correction method applied to two cases of real phase data taken simultaneously with the radiometer data at 183 GHz. One set of data was obtained at Mauna Kea between the JCMT and the CSO telescopes working in interferometer mode, at 356 GHz, which was kindly provided by Martina Wiedner from observations conducted during October 1998. The other set of data was obtained by us, using a 11.2 GHz 300-m baseline interferometer at Chajnantor, the selected site for ALMA.

2 Phase correction using 183 GHz data

2.1 Calculation of PWV

The theory of radiative transfer describes the behaviour of a flow of radiation propagating in a general class of media that absorbs, emit, and scatter the radiation. In the case of atmospheric propagation, we can neglect scattering. In this way we obtain a simple differential equation where the change in intensity, in an element of volume, is given solely by the absorption in the media plus any possible generation of energy within the volume. Furthermore, if we assume local thermodynamic equilibrium *i.e.* each point in the media is characterised by a temperature T, the source term corresponds to the Planck function.

At millimetre wavelengths $h\nu << kT$ for most temperatures, which is also known as the Rayleigh-Jeans regime, and the brightness temperature can be considered proportional to an equivalent blackbody temperature. One exception is the cosmic background emission that can not be represented accurately by the Rayleigh-Jeans approximation at 183 GHz because of its low brightness temperature. Under these conditions, if we observe with an ideal antenna a sector of the sky, free from emission other than the background radiation, the brightness temperature at a frequency ν is given by:

$$T_b(\tau_\nu) = T_{atm}\left(1 - e^{-\tau_\nu}\right) + \frac{h\nu}{k}\frac{1}{e^{h\nu/kT_B} - 1}e^{-\tau_\nu} \qquad (1)$$

Where h is the Planck's constant ($6.626076 \cdot 10^{-34}$ [Js]), k is the Boltzmann's constant ($1.38066 \cdot 10^{-23}$ [J/K]), T_B is the cosmic background temperature (2.7 [K]), τ_ν is the opacity or optical depth at frequency ν, and T_{atm} is the effective temperature of the atmosphere [K].

In equation (1), the first term of the right side is called the atmosphere brightness temperature. It represents the total effective brightness temperature of the atmosphere that, near 183 GHz, is due mainly to the thermal emission of the water vapour line.

The opacity τ_ν is a dimensionless function of the frequency ν, defined as the integral of the unit volume absorption coefficient k_ν along the total path s through the atmosphere.

$$\tau_\nu = \int_0^s k_\nu \, ds \qquad (2)$$

The absorption coefficient k_ν describes the interaction between the electromagnetic radiation and the atmospheric gases and depends not only on their atomic properties, but also on their pressure, density and temperature. It is equal to the sum of the unit volume absorption coefficients for each of the transitions of the gases constituting the atmosphere along the line of sight.

All real optical systems have some losses and the radiometer will not couple with 100% efficiency to the sky. In general, the response of a radiometer, called antenna temperature, is given by

$$T_A(\tau_\nu) = \eta\, T_b(\tau_\nu) + T_{amb}\left(1 - \eta\right) \qquad (3)$$

where η is the coupling efficiency to the sky.

The first term of the right side of equation (3) represents the brightness temperature, reduced by the coupling efficiency of the radiometer to the radiation coming from the sky, this term is detected through the main beam of the antenna. The second term represents the detected power through sidelobes and scattering from the ground, optics and surrounding structures at ambient temperature.

Here we calculate the atmosphere brightness temperature considering only the water vapour contribution, neglecting all other gases present in the atmosphere. In particular we do not consider oxygen with lines near 60 GHz and 118 GHz and the relatively narrow and weak ozone lines over 100 GHz. We follow the procedure outlined by Waters [3], were the absorption coefficient k_ν is calculated as the sum of two components: one due to the molecular line emission properties and the other an empirical correction term. The line shape utilised is the kinetic line shape.

The atmosphere is modelled as a discrete parallel atmosphere, with the troposphere divided in 15 equal layers of 200 m each. Since most of the water vapour is distributed close to the ground, calculations are done to a maximum altitude of 8 km. Radiation travels from the higher layers down with the brightness temperature of each layer calculated as the sum of two terms: one corresponding to the radiation entering the layer from layers above and the other term corresponding to the blackbody emission of the layer. Each layer is assumed to be of uniform density and at thermal equilibrium, with these conditions changing between layers. The cosmic background radiation is not considered at this stage of the calculations.

Under these assumptions, at each layer the brightness temperature is given by:

$$T_{brightness}(j) = T_{brightness}(j-1)e^{-k_v \Delta s} + T_j\left(1 - e^{-k_v \Delta s}\right) \qquad (4)$$

where $T_{brightness}(j)$ is the brightness temperature of the radiation entering the *j*-layer from layers above, k_v is the absorption coefficient of the *j*-layer, Δs is the distance travelled by the radiation through the *j*-layer, and T_j is the blackbody temperature of the *j*-layer

The calculation is started at the highest layer and proceeds to the last layer close to ground.

Ground based meteorological data (atmospheric pressure and temperature) serves as input to the model. The pressure assumed to vary with height according to the expressions:

$$P(h) = P_0\, e^{-\int_0^h \frac{1}{H(h)} dh} \qquad (5)$$

where $H(h)$ is the pressure scale height defined by:

$$H(h) = \frac{RT(h)}{M_d\, g} \qquad (6)$$

with P_0 the pressure at ground level [mbar], R the Molar gas constant, 8.31451 [J mole^{-1} K^{-1}], M_d is the molecular weight of "dry" air, 0.02896 [kg mole^{-1}], and g is the gravitational constant, 9.8 [m s^{-2}].

For the temperature, we assume that there is a 2% drop per kilometre from a temperature T_0 at ground level,

$$T(h) = T_0\,(0.98)^{h[\mathrm{km}]} \qquad (7)$$

The 183 GHz water line radiometers are of the heterodyne type, with three double sideband channels, with the channels spaced at 1.2, 4.1, and 7.6 GHz away from the line centre at 183.31 GHz. They have been described elsewhere [1, 4].

From initial observations, the response curve of the three IF channels as function of the amount of *PWV* was calculated using 1.5 km for the scale height of the water vapour distribution and over a wide range of meteorological variables. Under these conditions, the amount of *PWV* can be fitted accurately with a second order polynomial as function of the antenna temperature of the 7.6 GHz IF channel. This is explained in more details in a previous report [1], in particular we refer to Figure 6 there.

To start the program calculations we begin by estimating a seed value for the *PWV* from the antenna temperature of the 7.6 GHz IF channel. Assuming an exponential distribution of the water vapour density, the relation between the amount of *PWV* [mm], the water vapour density at ground level ρ_0 [kg/m^3], and the scale height of the water vapour distribution h [m] is given by

$$PWV = \int_0^s \rho_0\, e^{-s/h}\, ds \qquad (8)$$

Solving (8) for the water vapour density, the model is run from this starting value and a line strength is calculated. This value is then compared with the measured antenna temperatures at each of the IF channels, using equations (1) and (2), including the cosmic background contribution. Iterations are done over the water vapour density until a successful fit is achieved. Once a successful fitting for the water vapour density is obtained, the amount of *PWV* contained in the atmospheric column observed by the radiometer beam is obtained from (8).

For the case of Chajnantor, from radiosonde measurements we have determined that the average scale height is closer to 1.5 km, being smaller than the standard value of 2.0 km used extensively in the

literature. Also there is a possible diurnal change of its magnitude. This value should be determined for Chajnantor to have an accurate *PWV* statistics but it is not relevant on the calculations done here, were differential variations are relevant.

The *PWV* value estimated at (8), from antenna temperature measurements, is along the line of sight. This value can be normalised to zenith by multiplying by the sine of the elevation angle, *i.e.* dividing (8) by the number of atmospheres at the line of sight.

2.2 Phase correction

In simple terms, the amount of *PWV* is linearly related to an excess pathlength delay *L*, through the equation:

$$L = 6.3\,PWV \qquad (9)$$

with *L* and *PWV* in the same units [5]. This relation holds under the specific conditions of an isothermal atmosphere at 280 K and, for the case of Chajnantor, with lower atmosphere temperature the proportionality factor should be higher.

The excess pathlength variation between the two radiometers is calculated as:

$$\Delta L = 6.3\left(PWV_1 - PWV_2\right) \qquad (10)$$

These excess path delay variations ΔL translate to an equivalent phase variation $\Delta\phi$, at a wavelength λ, though the equation:

$$\Delta\phi = 360\frac{\Delta L}{\lambda} \qquad (11)$$

Because in the millimetre and submillimetre range the atmosphere is almost non-dispersive at frequencies away from the line centres, this equation allows us to calculate the phase variations due to the electrical pathlength variation at any frequency within this range.

2.3 Relative calibration between the two radiometers

In general, two independent radiometers observing the same piece of sky will give rise to different calibrated antenna temperatures. This unless special care is taken on assuring that the radiometer optics, as well as all other associated optics (*e.g.* telescope coupling optics), are identical, with all movable mirrors properly aligned. Also, care has to be taken to guarantee that the calibration loads are identical. In practice, not all variables can be controlled and different antenna temperatures will be obtained by different radiometers observing the same sky section.

Having different antenna temperatures at each radiometer, under the same meteorological conditions, will yield the atmospheric model to produce different values of *PWV* for each radiometer. This translates to an offset of the pathlength variations calculated using (10). This offset can be eliminated by a simple first order baseline removal of the data. In the case analysed here, we are using time intervals of 10 minutes to calculate the average of the phase data subtracting this value from the raw data.

2.4 Noise considerations

Ideally, the power measured by a radiometer is given by:

$$P = k\,B\left(T_A + T_{RX}\right) \qquad (12)$$

where T_A is the antenna temperature, and T_{RX} is the equivalent noise temperature of the receiver, k is Boltzman's constant, and B is the receiver bandwidth.

The receiver output, after downconversion, filtering, and amplification, is a voltage signal proportional to the power of this signal. This signal is processed by a voltage to frequency converter (V/F), which produces a frequency signal proportional to the power amplitude of the signal. This frequency is

integrated (counted) on buffers that are read by the computer at a fixed rate. For each channel, these values relate to the power *P* through:

$$IF = \alpha k B \left(T_A + T_{RX} \right) \qquad (13)$$

where *IF* is the uncalibrated total power response of one of the three IF channels of the radiometer as read by the computer, and α is the "conversion factor" of this channel. This conversion factor accounts for the power to voltage and voltage to frequency conversions; it is also function of the integration time.

The radiometer is calibrated continuously by measuring alternatively a hot and a warm load. Together with the sky measurements, we obtain a set of three values for each channel:

$$\begin{aligned} IF_{sky} &= \alpha k B \left(T_A + T_{RX} \right) \\ IF_{hot} &= \alpha k B \left(T_{hot} + T_{RX} \right) \\ IF_{warm} &= \alpha k B \left(T_{warm} + T_{RX} \right) \end{aligned} \qquad (14)$$

The difference between load readings can be calculated from

$$IF_{hot} - IF_{warm} = \alpha k B \left(T_{hot} - T_{warm} \right) \qquad (15)$$

Thus,

$$\alpha k B = \frac{IF_{hot} - IF_{warm}}{T_{hot} - T_{warm}} \qquad (16)$$

Solving for the antenna temperature in terms of measured calibration (load) parameters,

$$T_A = \frac{T_{hot} - T_{warm}}{IF_{hot} - IF_{warm}} IF_{sky} - T_{RX} \qquad (17)$$

with T_{RX},

$$T_{RX} = \frac{IF_{warm} T_{hot} - IF_{hot} T_{warm}}{IF_{hot} - IF_{warm}} \qquad (18)$$

All measured signals will have noise associated with them. If for the moment, we assume that all the calibration (load) measured quantities remain constant (or at least noise-free); the only noise source remaining is in the signal from the sky IF_{sky}. Thus, the noise amplitude in T_A will be given by:

$$\sigma_{T_A} = \frac{T_{hot} - T_{warm}}{IF_{hot} - IF_{warm}} \sigma_{IF_{sky}} \qquad (19)$$

This means that in the best case, when the only noise comes from the sky signal, we have a "fundamental limit" to the amplitude of the calibrated antenna temperature noise.

In (19), we assumed that all calibration quantities remained constant. In real life they all have noise and add to the noise budget of the calibrated antenna temperature calculated from the measured response of the radiometer. A way to reduce this effect is to average the load power response and the physical temperature readout of these loads.

In Figure 1 a) the antenna temperature for the 4.1 GHz IF channel of West radiometer is shown compared with the total power output of this same channel. The noise on the calibrated signal is evident. In Figure 1 b) we have the same antenna temperature calculated with a 60-s moving average over the total power response of the loads and their physical temperature readout. In this case, the noise level on the antenna temperature signal is reduced to the noise of the uncalibrated total power signal.

3 Measurements at Mauna Kea

3.1 Experimental set-up at Mauna Kea

The JCMT and the CSO are separated by a fixed baseline of 164 m. Interferometry is not the normal operating mode of these telescopes and thus the set-up of the 183 GHz radiometers is not really part of the routine operations. The observations used here were done by Martina Wiedner at a frequency of 356 GHz during October 24, 1998.

The 183 GHz radiometers used at Mauna Kea are similar to the ones used at Chajnantor, with small differences in the IF channel positions. The experimental set-up at Mauna Kea is best described in [6]. Here we will just recall that at both telescopes the 183 GHz radiometers are situated behind the main dish and share the main beam through an off-axis mirror. At the JCMT and the CSO the mounting scheme is different thus resulting in different responses to the sky signal.

The measured coupling efficiencies of the radiometers was 96% for the JCMT and 86% for the CSO [7], but the best fitting of the data could only be achieved by using a coupling efficiency of 88% for the JCMT and 92% for the CSO. With these values the difference between the predicted and the measured antenna temperature, in both radiometers, was always close to zero on the 1.2 and 7.8 GHz IF channels. The measured antenna temperature in the 4.2 GHz IF channel was always about 20% higher than the estimated value for both radiometers.

Our atmospheric water line fitting method needs the ground meteorological data as an input parameter. The weather data was not recorded during the observation period so we used constant values of T_{amb} = 273.16 K and P_{atm} = 600 mbar for the complete observation period [7].

3.2 Phase data at Mauna Kea

3.2.1 356 GHz interferometer data

The interferometer data file includes the relative phase between the CSO and the JCMT telescopes, as well as a time stamp. The recorded data covers a period of almost two hours and is sampled every 10 seconds.

It can be seen in Figure 2 that the interferometer phase fluctuations are stable around an average value during the first hour of observation, and a large drift during the last hour of observation. This drift has been attributed to thermal expansion of a cable, and is thus instrumental rather than atmospheric [7].

3.2.2 183 GHz radiometer data

The raw radiometer data file includes a time stamp and columns representing the antenna brightness temperature for each IF channel at each radiometer.

The data is collected as a 5-sec average per point. The time stamp of the radiometer observations and the recorded interferometer phase fluctuations does not coincide, thus we interpolated the estimated amount of *PWV* to coincide with the interferometer time stamp.

The amount of *PWV* is estimated from the antenna brightness temperature of the 7.6 GHz IF channel as described in the previous section. The result is shown in Figure 3. The amount of *PWV* measured at the CSO is consistently higher than the amount of *PWV* measured at the JCMT. The average ratio for the first hour of observation is 1.09±0.01. This means that there is either a calibration difference between both radiometers or a lower coupling efficiency to the telescope beam for one of the radiometers that will produce ground pick-up at ambient temperature. The absolute difference is not relevant in the phase correction scheme shown here because it will show up as a constant phase offset, and we are interested only in the deviations around the average value.

3.3 Phase correction at Mauna Kea

We analysed the first hour of the observation period, between 5 to 6 UT. The only data processing done is the removal of the average for each phase curve.

The phase variation curves measured by the two systems, shown in Figure 4, show the same trend but different amplitudes.

The standard deviation of the interferometer phase variation is $\sigma_{interferometer}$ = 64.45°. The standard deviation for the corrected phase, obtained by subtracting the radiometer phase variation from the interferometer phase variation, is $\sigma_{corrected}$ = 43.65°. The corrected phase is effectively decreased by 32% by subtracting the phase variations estimated from the 183 GHz water line measurements.

The correlation between the phase measured by the interferometer and the radiometer can be seen in Figure 5. The observed period shows a correlation:

$$\Delta\phi_{interferometer} = 0.0048 + 1.4359\,\Delta\phi_{radiometer} \qquad (20)$$

with a correlation coefficient of 0.7722.

4 Measurements at Chajnantor

4.1 Experimental set-up at Chajnantor

There are two interferometers at Chajnantor, one installed by NRAO and the other one installed by ESO. Each interferometer has two 1.8-m antennas separated by a 300-m baseline, observing a 11.2 GHz beacon from a geostationary satellite. After downconversion the signal from one of the antennas is phase locked to the satellite beacon. Further downconversion and digitising is done, before extracting the relative phase between both signal streams [8]. We have placed a 183 GHz water vapour line radiometer close to each antenna element of the ESO interferometer. These radiometers, built in a collaborative effort between Onsala Space Observatory and the Mullard Radio Astronomy Observatory, have been described before in [1, 4]. The amount of *PWV* in the line of sight is determined as described in section 2.1. During the measurements described here the 183 GHz water vapour radiometers are looking at the satellite observed by the NRAO interferometer, because of some problems with the ESO interferometer. This is not the ideal situation because the distance between the NRAO interferometer antennas and the radiometer is about 6 meters, compared with about 2 meters between the ESO interferometer and the radiometer. This separation is along the N-S direction, while the interferometer baseline is along the E-W direction.

In order to compare the phase variations measured by the interferometer and those estimated from radiometric measurements, we need to observe the same atmospheric column. This is done by pointing the steerable mirror of the radiometer towards the direction of the satellite observed by the interferometer.

To improve the alignment of the radiometer and interferometer antenna beams, we used the solar eclipse produced by the motion of the satellite in front of the sun during its transit between hemispheres in the days around the equinox. This event leaves a clear signature in the interferometer response (Fig. 6). By maximising the total power level of the radiometers at the same time, we can align the radiometer beams with the interferometer beams.

The jump in the radiometer power output signal is caused by the loss of lock of the received satellite signal [9]. Nevertheless, we can fit a Gaussian distribution to the phase-locked signal and obtain the half power beamwidth (HPBW) of the interferometer beam. This was done for one of the channels and results in a HPBW of 1.02º. This compares very well with 1.05º as predicted from diffraction theory, using a dish diameter of 1.8 m and an operating frequency of 11.2 GHz. The transit time in front of each interferometer antenna can be calculated from Figure 6 by determining it from the centre peak. This results in a transit time difference of 41.18 seconds between the two antennas. This time difference translates to an angular displacement of 10’ between the interferometer antennas.

Also a Gaussian fit can be done to the power response of the radiometers to the transiting sun (Fig. 7). This gives a HPBW of 2.59º for the West radiometer and 2.52º for the East radiometer. The transit time difference for the two beams gives a relative angular displacement of about 3.5’ between the beams of the two radiometers.

The angular size of the satellite is much smaller than the average angular size of 0.53º of the sun thus the accuracy of the method is limited to about 0.5º. The comparison of the average transit time of the interferometer and the average transit time of the radiometers gives an average angular displacement of 27' between the two beams. This value is within the experimental accuracy of the method.

Despite the good relative pointing of the two instruments, there is still a significative mismatch in the beam sizes. Because of the different HPBW, at a distance of 1,000 m (corresponding to a height of the order of 500 m) the interferometer beam diameter will be of the order of 20 m, whereas the radiometer beam will have about 50 m diameter.

By performing measurements of antenna temperature at different elevation angles, and fitting least squares to the antenna temperature as function of elevation, it is possible to obtain the coupling efficiency to the sky. A coupling efficiency of η = 97% was found for the West radiometer, and η = 98% for the East radiometer.

4.2 Phase data at Chajnantor

4.2.1 11.2 GHz interferometer data

The raw interferometer data, sampled at a 1-second rate, is divided in 10-minute periods. To remove long term drifts in the phase, caused by the orbital drift of the satellite from the antenna beam centres and instrumental drifts, a second order baseline is removed from the data sets.

4.2.2 183 GHz radiometer data

The raw radiometer data files, one for each radiometer, include a time stamp and columns representing the uncalibrated total power response for each IF channel. The file is read by a C program, running on a PC compatible, which calculates the antenna brightness temperatures and estimates a value of *PWV*. A new file is written, keeping the time stamp and adding columns for the zenith *PWV*, the line of sight *PWV*, the path delay, the zenith opacity and brightness temperatures for each IF channel. As described in section 2.4, to reduce the noise on the *PWV* estimation, before performing the antenna temperature calibration we calculated moving averages of 60 sec on the values of the physical temperature reading of the loads as well as on the radiometric total power readings of these loads.

The radiometer data is sampled every 2 seconds. Since this time stamp does not coincide with the recorded interferometer phase fluctuation, we interpolated the resulting estimated amount of *PWV* to coincide with the radiometer time stamp (2-sec time series). A file with the time stamp and columns for the phase variation in the interferometer and the radiometer is generated.

The radiometer at the West side of the baseline has been in operation since September 1998. The radiometer at the East side was made operational only late March 1999.

4.3 Phase correction at Chajnantor

Here we will concentrate on the data obtained on November 15, 1999. The time series for this day is divided in 10-minute periods and, after a linear baseline removal of the radiometer data, both signals are correlated using least squares fitting to a linear relation between the interferometer phase (independent variable) and the radiometer phase (dependent variable).

$$\Delta\phi_{radiometer} = a + b\,\Delta\phi_{interferometer} \qquad (21)$$

Ideally the offset coefficient *a* should be zero, the linear coefficient *b* should be one, and the correlation coefficient between both time series should also be one.

The degree of correlation varies during the day from no correlation (correlation factor close to zero) to high correlation (correlation coefficient close to unity). The slope that ideally should be unity varies also during the day, indicating that the proportionality factor used in equations (9) and (10) is not the correct one. It seems that this proportionality factor might also be varying during the day.

In Figure 8, we show the result for November 15, 1999. The two upper plots on the figure show the phase variation measured with the interferometer and the radiometer respectively. These two time

series are not identical, something that is reflected in the centre plot that shows the correlation over the day for sample 10-minute periods. In this particular example, during the first quarter of the day, there is no correlation, while during the second quarter, the correlation is marginal, and during the last half of the day, the correlation improves.

The corrected phase is obtained by subtracting the radiometer phase from the interferometer phase. By comparing the variance of the interferometer phase and the corrected phase, the phase improvement can be quantified. During the observed day, the phase improvement ranges from zero at the first quarter, to 36% at the centre, and 53% during the last half of the day.

5 Conclusions and future work

In measurements done at Mauna Kea, using the JCMT and the CSO telescopes as an interferometer, at an altitude of 4,200 m and an operating frequency of 356 GHz, the phase variation was decreased by 32% using this method. The correlation between the phase variation measured by the interferometer and the one radiometricaly estimated is very good. The slope of the linear fitting shows that there is a scale discrepancy between the relative amplitude of the phase variations from the two instruments. At Mauna Kea, this can be explained either by a wrong result of the line fitting process, that is able to reproduce accurately the variations but not the correct *PWV* scale, or by a wrong proportionality factor between the amount of *PWV* measured and the pathlength variation (equations 9 and 10).

In the data from Mauna Kea, the time stamp on the phase variation readings was different for the radiometer and for the interferometer data. In addition, the integration time is different on the two databases. In order to proceed with the analysis we had to interpolate the value of *PWV* (or excess path delay) to the nearest time value coinciding with a value of phase for the interferometer. The interferometer data is sampled every 10 seconds and the radiometer data every 5 seconds. The error in time between readings can be as large as 5 seconds. This should be corrected in order to improve the correlation between phase measured in both systems.

At Mauna Kea the observations are conducted at 4,200 m, where the atmosphere is complex, with possible clouds or layers of water in liquid phase. This is not considered for the moment in our line-fitting model. At Chajnantor the water inside the clouds is expected to be mostly frozen.

At Chajnantor, the amount of *PWV* contained in an atmospheric column has been estimated from a set of antenna brightness temperatures obtained by two 183 GHz water vapour monitors measuring in the same direction as the two elements of a 11.2 GHz interferometer. This estimation is done for every measurement at a 2-sec rate, thus generating a time series for the *PWV* variation during the day. The differential variation of *PWV* is translated to a time series of phase variation using a linear relation scalable to any frequency within the millimetre wavelength range.

The phase improvement of more than 50% obtained at Chajnantor, during the second half of the day is very encouraging. There are some anomalies that need to be explained in the phase variation data that differs between the two instruments at some times of the day.

The anomalies seen in the interferometer phase variation at Chajnantor during the first part of the day 15/11/99 (Figure 8), seem to be real because they can also be seen with the ESO interferometer that is observing another satellite at a different elevation angle. This discards antenna movements due to wind or electromagnetic interference as origin of these fast fluctuations, since it is very unlikely that the same effect can be seen at both interferometers at the same time. Investigation on this phenomenon is currently underway.

There is a clear indication that there is a difference between the amplitude of the phase measured with the interferometer and the one estimated from radiometric measurements. At Chajnantor this difference seems to vary along the day and more data is needed to understand this variation. A more rigorous approach is to consider the temperature dependence of the phase-path length relation.

Another area that should be investigated is the water line fitting, since we are using a simple atmospheric model based in the Waters method [3] considering only the wet air contribution, plus an empirical correction factor. A more detailed study of the accuracy of the fitting needs to be done, considering different meteorological conditions.

Acknowledgements

The authors warmly acknowledge the help from Martina Wiedner formerly at MRAO, now at the Harvard-Smithsonian Center for Astrophysics, who kindly provided the data from Mauna Kea.

One of the authors (GD) acknowledges the fundamental contribution of Javier Brahm, MD and Erwin Buckel, MD for making possible at all the participation of this author on the work.

Important part of the funding for this project came out of the budget of Onsala Space Observatory provided by the Swedish Natural Science Council (NFR).

References

[1] G. Delgado, A. Otárola, V. Belitsky, D. Urbain, P. Martin-Cocher, "The Determination of Precipitable Water Vapour at Llano de Chajnantor from Observations of the 183 GHz Water Vapour Line," ALMA Memo Series No. 271, 1999.

[2] P. Jarlemark, "Analysis of Temporal and Spatial Variations in Atmospheric Water Vapor Using Microwave Radiometry," Technical Report No. 308, Chalmers University of Technology, 1997.

[3] J. Waters, "Absorption and emission by atmospheric gases," in *Methods of Experimental Physics*, M. Janssen (Ed.), Vol. 12B, pp. 142-176, 1976.

[4] http://gard04.mc2.chalmers.se/183GHz_radiometer.htm

[5] A. Thompson, J. Moran, and G. Swenson, *Interferometry and Systhesis in Radio Astronomy*, Krieger Publishing Company, 1994.

[6] M. Wiedner, PhD thesis, University of Cambridge, 1998.

[7] M. Wiedner (mwiedner@randonnee.harvard.edu), private communication.

[8] S. Radford, G. Reiland, and B. Shillue, "Site Test Interferometer," PASP, Vol. No. 108, pp. 441-445, 1996.

[9] S. Radford (sradford@nrao.edu), private communication.

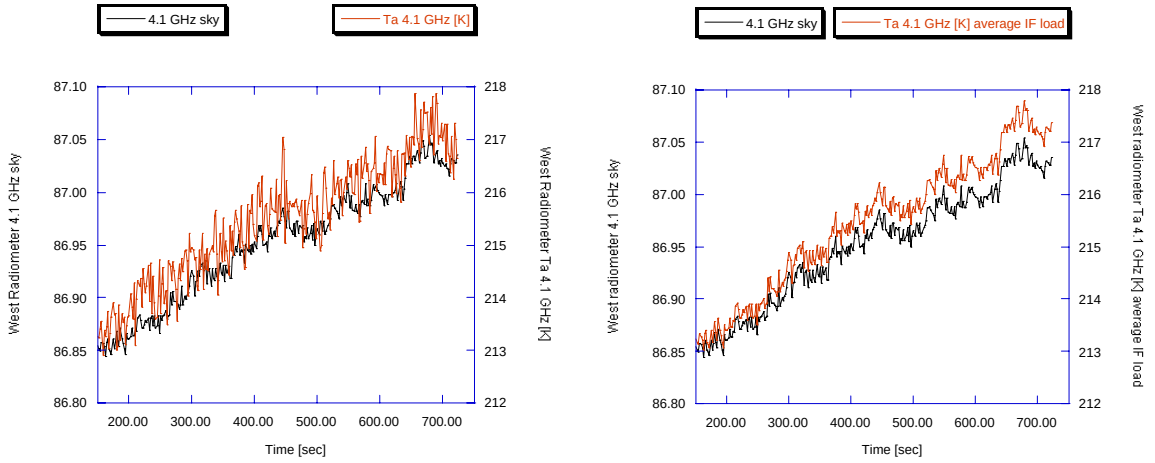

a) b)

Fig. 1 Total power for the 4.1 GHz IF channel (black curve) and associated calibrated antenna temperature (red curve), for a) non-averaged calibration load signals and b) 30-s averaged calibration load signals

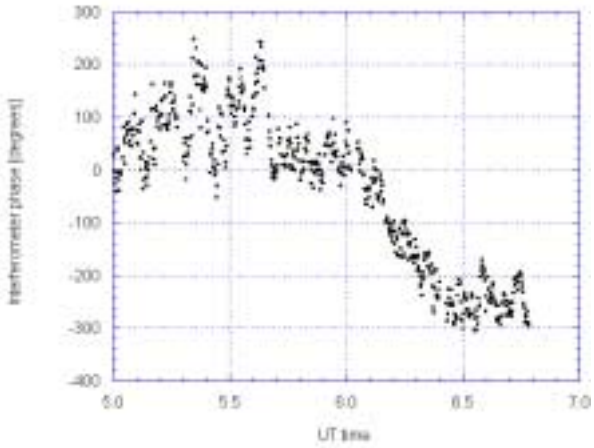

Fig. 2 Phase fluctuation between the CSO and the JCMT telescopes operating in interferometer mode

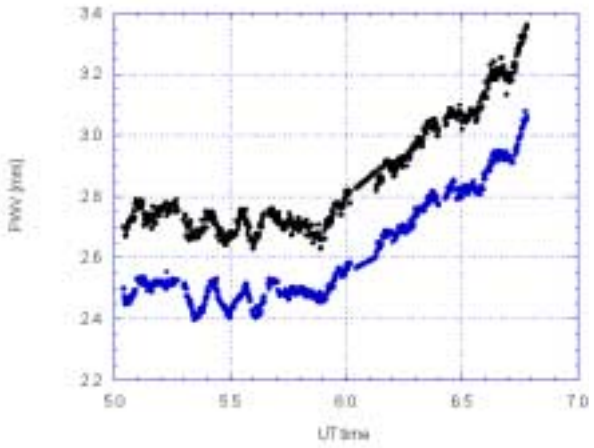

Fig. 3 Estimated amount of *PWV* in the direction of observation for the CSO (upper black curve) and the JCMT (lower blue curve)

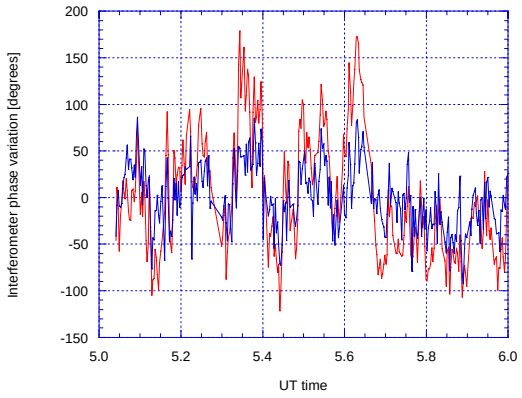

Fig. 4 Phase variation for the 183 GHz water vapour radiometers (lower blue curve) and the interferometer (upper red curve).

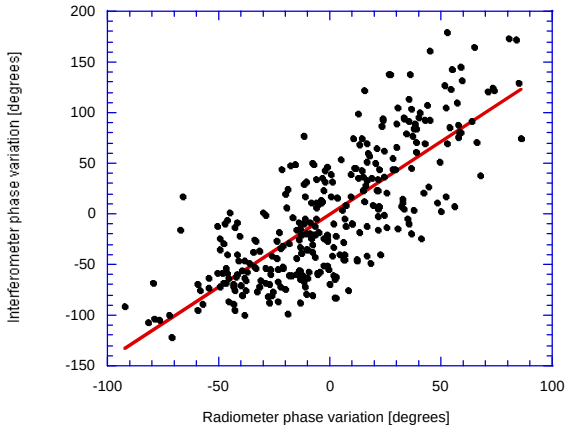

Fig. 5 Correlation between the interferometer phase variations and the radiometer phase variations

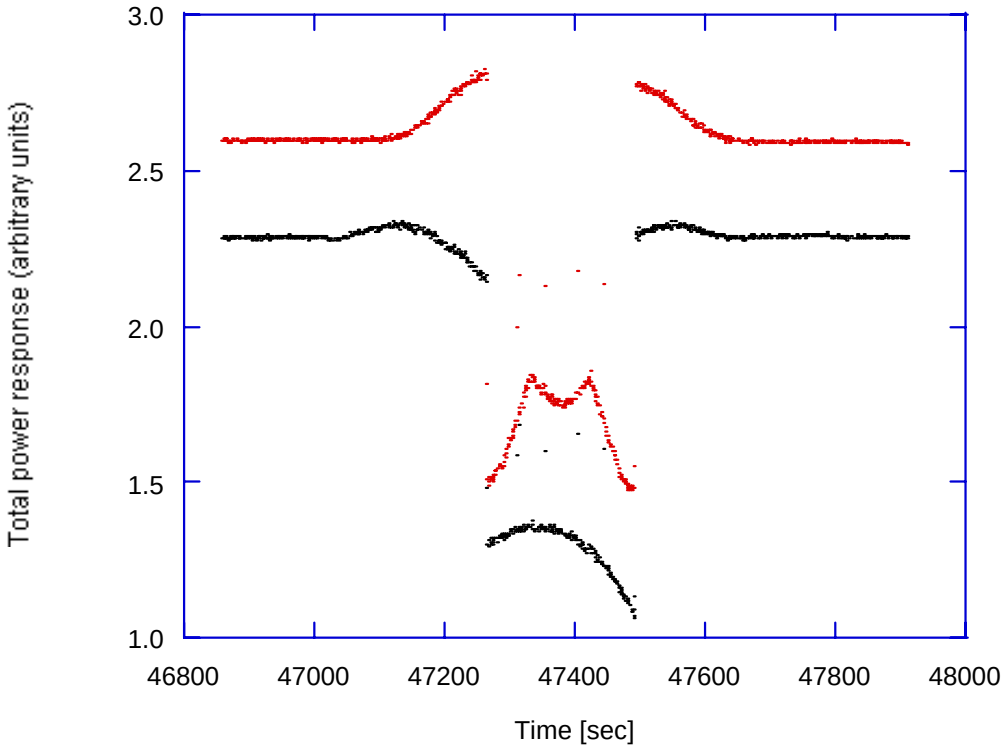

Fig. 6 Signature of the satellite eclipse on the interferometer signals

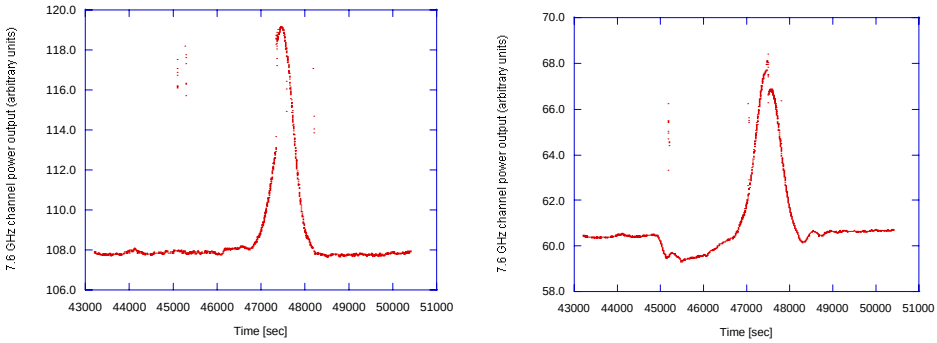

Fig. 7 Total power response of the 183 GHz radiometers

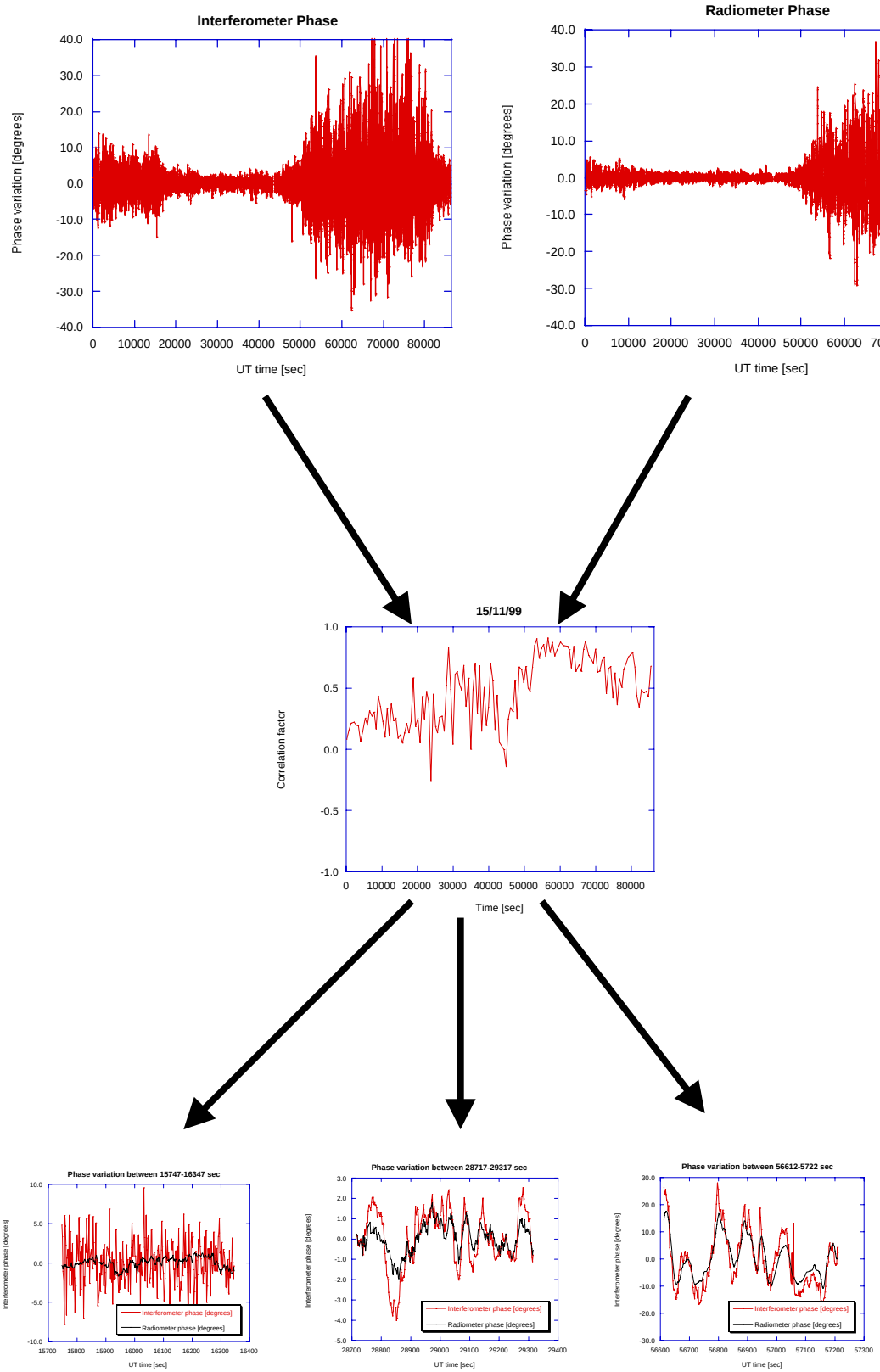

Fig. 8 Correlation for day 16/11/99 at Chajnantor. The upper plots show the time series of interferometer phase (left) and radiometer phase (right for the complete day. The centre plot shows the correlation between these two time series, while the three lower plots show a 10-minute detail of both phase variations at different correlation factor values.